

Electron-vacancy scattering in SrNbO₃ and SrTiO₃: A density functional theory study with nonequilibrium Green's functions

Victor Rosendal ¹, Nini Pryds,¹ Dirch H. Petersen ¹ and Mads Brandbyge²

¹*Department of Energy Conversion and Storage, Technical University of Denmark, 2800 Kongens Lyngby, Denmark*

²*Department of Physics, Technical University of Denmark, 2800 Kongens Lyngby, Denmark*



(Received 12 January 2024; revised 5 April 2024; accepted 26 April 2024; published 13 May 2024)

Oxygen vacancies are often attributed to changes in the electronic transport for perovskite oxide materials (ABO₃). Here, we use density functional theory coupled with nonequilibrium Green's functions to systematically investigate the influence of O vacancies and also A- and B-site vacancies, on the electronic transport as characterized by a scattering cross section. We consider SrNbO₃ and *n*-type SrTiO₃ and contrast results for bulk and thin film (slab) geometries. By varying the electron doping in SrTiO₃ we get insight into how the electron-vacancy scattering varies for different experimental conditions. We observe a significant increase in the scattering cross section (in units of square-lattice parameter a^2) from ≈ 0.5 – $2.5a^2$ per vacancy in SrNbO₃ and heavily doped SrTiO₃ to more than $9a^2$ in SrTiO₃ with 0.02 free carriers per unit cell. Furthermore, the scattering strength of O vacancies is enhanced in TiO₂ terminated surfaces by a factor of more than 6 in lowly doped SrTiO₃ compared to other locations in slabs and bulk systems. Interestingly, we also find that Sr vacancies go from being negligible scattering centers in SrNbO₃ and heavily doped SrTiO₃, to having a large scattering cross section in weakly doped SrTiO₃. We therefore conclude that the electron-vacancy scattering in these systems is sensitive to the combination of electron concentration and vacancy location.

DOI: [10.1103/PhysRevB.109.205129](https://doi.org/10.1103/PhysRevB.109.205129)

I. INTRODUCTION

The plethora of material properties that perovskite oxides (ABO₃) offer is rewarding both for applications and also from a fundamental point of view. The behavior of these materials emerges from the complex interaction among atomic, electronic, and lattice degrees of freedom, and perovskite oxide materials show many exotic properties that can be controlled by tuning the chemical composition. Through optimized growth procedures, to limit defect formation, oxide films can exhibit highly mobile electrons [1]. More specifically, it has been shown both experimentally and theoretically that the oxygen content is crucial for the electronic structure and properties of oxides [2,3]. The disorder due to oxygen vacancies has been connected to the poor or even insulating electronic behavior of thin film oxides [4–8]. On the other hand, O vacancies are known to form *n*-type SrTiO₃, and they have even been attributed to the formation of highly conducting two-dimensional electron gases at the interface between insulating oxides [9]. This suggests that O vacancies both result in free electrons and also act as scattering centers. Furthermore, both A- and B-site vacancies/disorder have been correlated with electrical properties in perovskite oxides [6,10,11]. In other words, it might be important to consider the different types of vacancies and their relative importance might not be universal. Moreover, since the experimental studies are often based on thin films, the role of finite thickness should be considered. The thickness of the film could influence the vacancy formation, but perhaps also the scattering strength of one vacancy. The exact relation between vacancies, film thickness, and the electron mobility still remains to be explored.

An oxide of recent interest is SrNbO₃ [12]. The interest stems from the potential to use SrNbO₃ as a transparent conductor [13] or even to realize extremely mobile electrons by forming semi-Dirac dispersions [14]. These findings make it worthwhile to ask what the effects of different vacancies are on the electronic transport properties in a material such as SrNbO₃. Furthermore, experiments suggest that the carrier concentration of conducting oxides is thickness dependent [15,16], which leads to the question of whether this has a significant impact on the behavior of the electron-vacancy scattering.

To answer these questions, we examine the influence of vacancies on the electronic transport in SrNbO₃ and *n*-type doped SrTiO₃ using density functional theory (DFT) based calculations. We employ nonequilibrium Green's functions (NEGFs) to remove periodic boundary conditions (PBCs) and to study transport. Both bulk and slabs are considered, and different vacancy types and positions are sampled. To investigate the importance of carrier concentration, we systematically vary the electron count of SrTiO₃ by alloying with V within the virtual crystal approximation (VCA).

We show that the vacancies reduce the electron transmission, and hence conductance, as expected. More interestingly, we note how O vacancies have a rather small scattering cross section and resistance, compared to Nb or Ti vacancies. Furthermore, we find that decreasing the electron concentration in SrTiO₃ leads to a significant increase in the scattering cross section of Sr and Ti vacancies, while O vacancies are not affected as much. This suggests that A- and B-site vacancies might play a large role in the electronic behavior of thin film oxides, especially in conditions where the carrier concentrations are depleted in the thin films. Moreover, slabs show

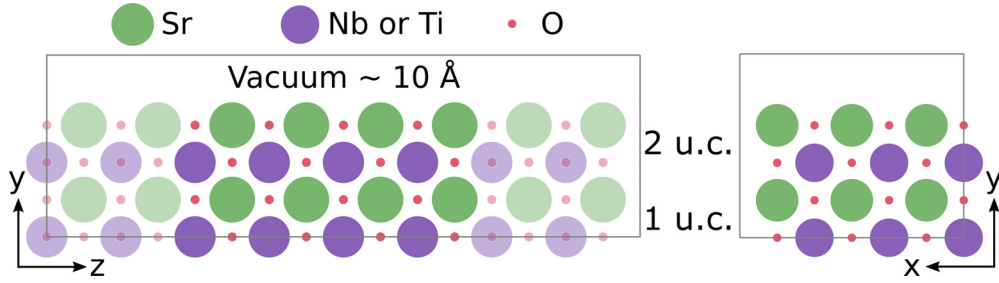


FIG. 1. Schematic of the transport problem of the two u.c. thick slab of SrNbO₃ or SrTiO₃. The transport is in the z direction and repetition of three u.c. is used in the x direction to reduce the vacancy-image interaction. The transparent circles denote the “left”/“right” electrode regions. The vacancies are placed at the center of the scattering region. Note that the vacuum region is shrunk for visualization purposes. The unit cells are counted starting from the NbO₂ or TiO₂ termination.

steps in the energy-resolved conductance due to confinement effects. Interestingly, we find that TiO₂ terminated surfaces show enhanced O vacancy scattering cross sections, compared to bulk and other layers.

II. METHOD

The PBE [17] DFT functional was used throughout the paper. We note that some transition metal oxides require beyond DFT to predict the correct electronic phase, e.g., metal vs insulator. However, both experiments [12,13] and dynamical mean-field theory calculations [13,18] indicate that SrNbO₃ is in fact metallic as predicted by band theory. In any case, we performed a few calculations of both pristine and defective (with O vacancy) two unit cells (u.c.) slabs of SrNbO₃ with a Hubbard U correction. We sampled values up $U_{\text{eff}} = U - J = 5 - 0.8$ eV. All configurations were conductive and the U had a minor influence on the electron-vacancy scattering. To reduce the computational cost and to ease the numerical convergence, we stay at the DFT level, i.e., no further DFT + U calculations were performed. To study the electron transport we use NEGFs, in which one separates the “scattering” region (colorful circles in Fig. 1) from the semi-infinite “electrode” regions (transparent circles in Fig. 1). We consider both SrNbO₃ and SrTiO₃ doped with electrons by mixing the pseudopotential of Ti and V within the VCA [19]. The electrodes are pristine (bulk or slabs) cells and act as infinite reservoirs where the electrons are in (local) equilibrium described by a temperature and chemical potential. The scattering region contains repetitions of the perovskite oxide cells along the transport direction (z), but now with a vacancy included. This is where the periodic translational symmetry of the lattice is broken and a resistance emerges. PBCs are applied in the transverse x and y directions (we use three u.c. in both directions in bulk and three u.c. in the x direction in slabs). Therefore, the defect-defect distance is three unit cells in the transverse directions. This was a compromise between the cost and accurate description of *local* point defects. In the x, y directions we employed 12 k points (per unit cell) for the calculation of self-consistent charge densities, while the transmission functions were calculated using 60 k points (per unit cell). In the NEGF technique the semi-infinite “left/right” electrodes are coupled to the central region via left/right self-energy terms. In practice the calculations were done using SIESTA [20] and TRANSSIESTA [21,22] which use linear

combination of atomic orbitals (LCAO) basis sets which we benchmark against plane-wave calculations. A comparison between the LCAO and plane-wave band structures can be found in Supplemental Material [23]. The vacancies were introduced as “ghost atoms” (LCAO atoms without pseudopotentials). Transmission functions were calculated based on the self-consistent electronic structure using TBTRANS [22] and postprocessing was done using SISL [24] codes.

The electrodes were two unit cells in transport direction, which is necessary to make sure there are only matrix elements between orbitals up to nearest neighbor electrode cells. Furthermore, the NEGF formalism requires that the connection between the electrodes and the first layer in the transport direction of the central region is “bulklike” and not perturbed by the defect. In other words, there should be an extension of the central region that is identical to the the electrode region where the perturbation caused by the defect can vanish. For this reason, we chose to use a central region of four unit cells in the transport direction (see Fig. 1). In the slab calculations, a vacuum of 10 Å was introduced to separate the slab from its images. The slabs were chosen to be asymmetric. Due to the asymmetry of the slabs and periodicity in y direction, we employed a slab dipole correction out of plane to compensate for the artificial electrostatic interaction between the two sides of the slabs.

The cubic phases of SrNbO₃ and SrTiO₃ were used with lattice parameters of $a = 4.0182$ and 3.8958 Å, respectively, as predicted using DFT [18]. Note that we do not consider the change in lattice parameter when electron doping SrTiO₃. Furthermore, we do not systematically relax the ionic degrees of freedom. This simplification is motivated by the fact that a relaxation did not affect the transmissions significantly in two u.c. SrNbO₃ without or with O, Nb, or Sr vacancies (see Supplemental Material [23]).

In this paper, we limit ourselves to zero bias conditions, i.e., the linear response regime. The transmission function from left to right electrode takes the form

$$T_{LR} = \text{Tr}[\mathbf{G}\mathbf{\Gamma}_L\mathbf{G}^\dagger\mathbf{\Gamma}_R] \quad (1)$$

where \mathbf{G} is the retarded Green’s function in the scattering region determined from overlap (\mathbf{S}) and Hamiltonian (\mathbf{H}) matrices in the scattering region,

$$\mathbf{G} = [(E + i0^+)\mathbf{S} - \mathbf{H} - \mathbf{\Sigma}_L - \mathbf{\Sigma}_R]^{-1}, \quad (2)$$

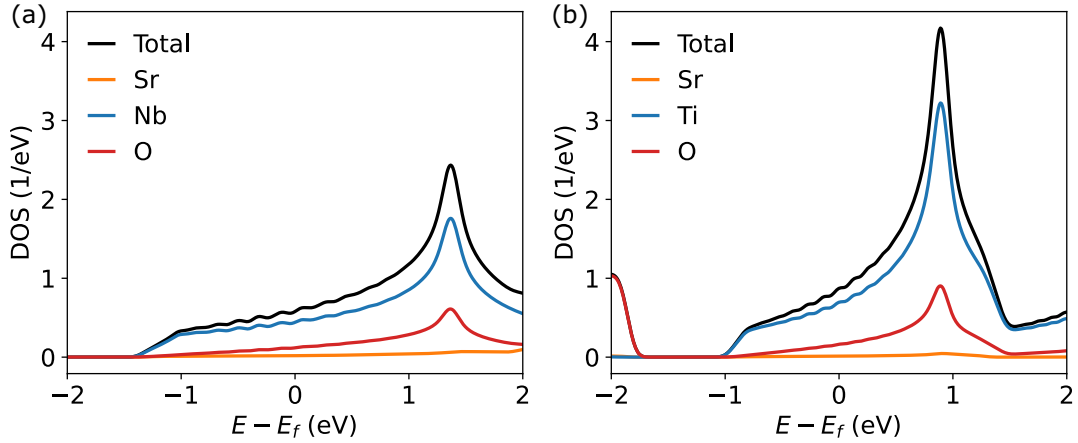


FIG. 2. Atom projected DOS of bulk SrNbO₃ and SrTiO₃ doped with 1 $e/u.c.$ The DOS is given for the five atom unit cell. Conduction bands have strong Nb/Ti and O character.

and $\Gamma_{L/R}$ is the “level broadening matrix” due to the left or right electrodes:

$$\Gamma_{L/R} = i[\Sigma_{L/R} - \Sigma_{L/R}^\dagger]. \quad (3)$$

We have omitted the energy and momentum variables for simplicity. In Eqs. 2 and 3, the electrode self-energy is denoted $\Sigma_{L/R}$. We present our results using the conductance function, $G(E) = \frac{e^2}{h} T_{LR}(E)$, normalized with the cross-sectional (xy) area of the conductor, A , in units of primitive unit cell area (a^2). The conductance is given per spin channel, there are therefore two identical channels with equal conductances since we perform unpolarized calculations. We note that we have observed a small spin selective electron-vacancy scattering when spin-polarized calculations were performed. However, while this could be an interesting direction for future studies, we neglect this effect due to the computational complexity and observed sensitivity to ionic relaxation. We reiterate that we did not further consider spin polarization in this paper.

III. ELECTRONIC STRUCTURE OF SrNbO₃ AND SrTiO₃

Charge is conducted by electrons near the Fermi level (E_F) and it is therefore insightful to examine the electronic structure in the vicinity of the Fermi level. To do this, we calculated the atomic projected density of states (PDOS) of bulk SrNbO₃ and SrTiO₃ doped with $1e/u.c.$ The PDOS is shown in Fig. 2. Note that the results correspond to the cubic five atom unit cells without any vacancies. Therefore, these states that will conduct charge in the pristine cases. The conduction bands are qualitatively similar; however, the bandwidth is substantially larger for SrNbO₃ compared to SrTiO₃. This is due to the more delocalized character of the Nb $4d$ states compared to the smaller Ti $3d$ states. To a large extent, the conduction bands originate from the atomic orbitals of the B -site ions (Nb and Ti). There is also a substantial contribution from the O orbitals, while the contribution of Sr on the conduction bands is negligible. From the PDOS, we expect the materials to be conducting, and that the conduction will be done by the B -site d states that are bridged by the O ($2p$) states. The

atomic origins of the states (naively) suggest that B -site and O vacancies should dominate the scattering.

The PDOS in Fig. 2 was calculated using LCAO DFT, which agrees very well with previous plane-wave DFT (see [18] and Supplemental Material [23]). Furthermore, recent comparisons between plane-wave DFT and angle-resolved photoemission spectroscopy show good agreement [25,26]. This gives us confidence in the LCAO description used here. We note that in both aforementioned studies hole doping was likely observed, likely due to vacancies.

IV. ELECTRON TRANSPORT IN SrNbO₃

We begin by examining the electron transport in bulk and slabs of SrNbO₃. We will use this as the baseline for conducting d^1 perovskite oxides, i.e., systems with very high electron concentration and good electrostatic screening. The influence of carrier concentration will be considered in the subsequent section.

A. Bulk conductance in SrNbO₃

Figure 3(a) shows the area specific electrical conductances for bulk SrNbO₃ with different vacancies. While charge is conducted mainly by electrons very close to the Fermi level (E_F), we show a larger range of energies. As expected, there is good conduction in pristine SrNbO₃ near the Fermi level due to the wide conduction bands originating from hybridized Nb $4d$ and O $2p$ states. Introducing vacancies reduces the conductance per area around E_F by 10–30%, as shown Fig. 3(a). In other words, a vacancy causes resistance. Furthermore, we observe that introducing a vacancy in a NbO₂ layer (i.e., Nb vacancy or O vacancy between Nb ions in the transport direction) causes more resistance than a vacancy in a SrO layer (i.e., Sr vacancy or O vacancy between Nb ions perpendicular to the transport direction). This is expected due to the origin of the conduction states in SrNbO₃ mentioned earlier, i.e., the conduction is done by Nb states “connected” by O states.

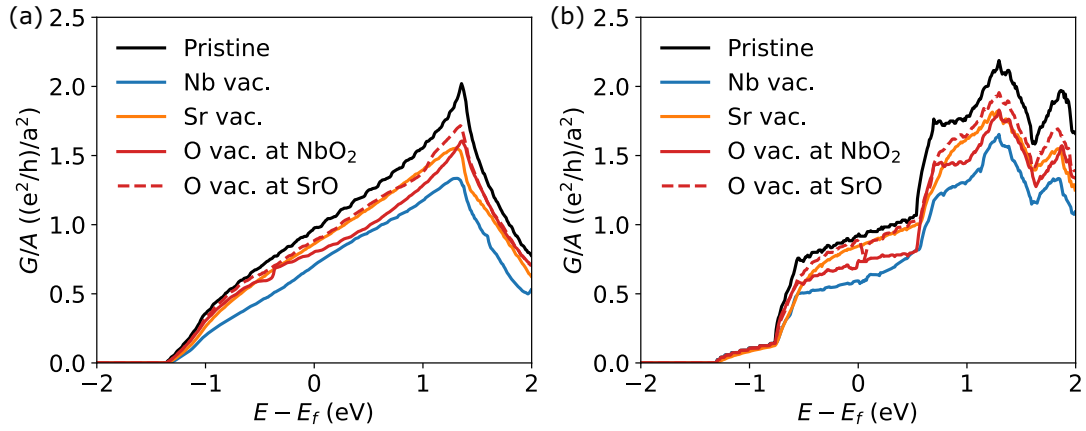


FIG. 3. Conductance per unit cell area for different vacancy configurations. (a) Bulk SrNbO₃ with periodic boundary conditions in the transverse (xy) directions and a three u.c. supercell. (b) Two unit cell thick slab configuration of SrNbO₃. The vacancies are placed in the first u.c. counting from the NbO₂ termination layer. Periodicity is applied in the transverse (x) direction using a three u.c. supercell.

B. Slab conductance in SrNbO₃

Next, we investigate the impact of confinement and surface (present in slabs) on the conductive properties of SrNbO₃. Asymmetric slabs of two, three, and four u.c. SrNbO₃ were investigated. Figure 4 shows the conductance for two, three, and four u.c. slabs of pristine SrNbO₃. The confinement leads to large jumps in the conductance depending on the slab thickness due to the quantization transverse to the slab plane. In Fig. 3(b), the conductances of a two u.c. slab of SrNbO₃ with different vacancies are shown. Here, we consider vacancies placed within the first unit cell on the NbO₂ terminated side (see Fig. 1). Other vacancy locations will be discussed later. We find that the trend in scattering seen as a drop in conductance is quite similar to the bulk cases; vacancies in a SrO layer are much less disruptive for electron transport than those in an NbO₂ layer. Qualitatively, vacancies placed in the second u.c. from the NbO₂ termination (see Fig. 1) show similar trends in resistances, or drops in conductances. For quantitative comparisons, we refer to the following section.

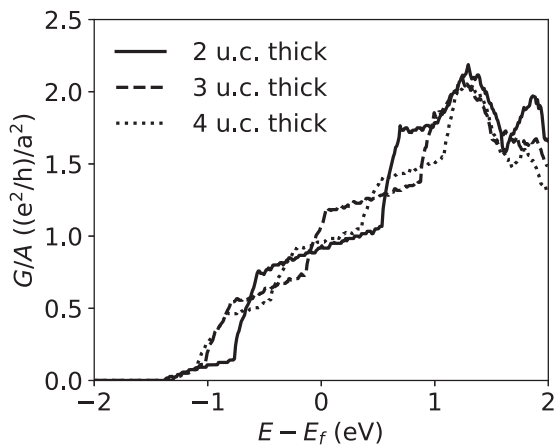


FIG. 4. Conductance of pristine SrNbO₃ slabs with varying thickness. The out-of-plane confinement of the electron wave function leads to sharp steps in the conductance. The finite slopes remain due to the in-plane PBC (i.e., in the x direction in Fig. 1).

C. Vacancy scattering cross sections in SrNbO₃

Having shown the energy resolved conductance for bulk and one slab configuration of SrNbO₃, we now extract the scattering cross sections from vacancies placed in bulk and slabs of different thicknesses at different locations. We define the scattering cross section as

$$\sigma_s = A[T_0(E_F) - T_d(E_F)]/T_0(E_F) \quad (4)$$

where A is the geometrical cross section, and T_0 and T_d are the area-specific transmissions of the pristine and defective system, respectively [27,28]. The scattering cross section gives an intuition of how much of the cross-sectional area is effectively lost due to the introduction of the vacancies. This is done for a certain transverse supercell, hence its maximum value will be A corresponding to a blocked, nontransmitting supercell. With this definition of cross section we will get a lower estimate. Moreover, the definition of the geometrical cross section, A , is not obvious when comparing bulk and slabs. We have defined A using the ionic locations, which neglects any conduction done slightly into the vacuum of the slabs. Therefore, comparison between bulk and slab scattering cross sections should be done while keeping in mind that the results are sensitive to our definition of A . Note that due to the finite sampling of the transmission functions there might be numerical artifacts which could propagate into the evaluated scattering cross sections. Therefore, we smear the transmissions with the energy derivative of the Fermi-Dirac distribution at 300 K. This is only done when evaluating scattering cross sections and subsequent quantities (e.g., mobility later on).

Figure 5 presents the scattering cross sections for two and four u.c. SrNbO₃. For simplicity, the results of three u.c. are omitted. Different transverse locations in the slab (i.e., different unit cells in the y direction in Fig. 1) and vacancy types are sampled. Furthermore, the bulk values are shown as horizontal lines. As noted above the trend is similar for bulk and slab configurations and there is no strong layer dependency on the scattering strengths, except for the O vacancy positions where the oscillating behavior of the O scattering cross section depicts the difference in scattering strength from

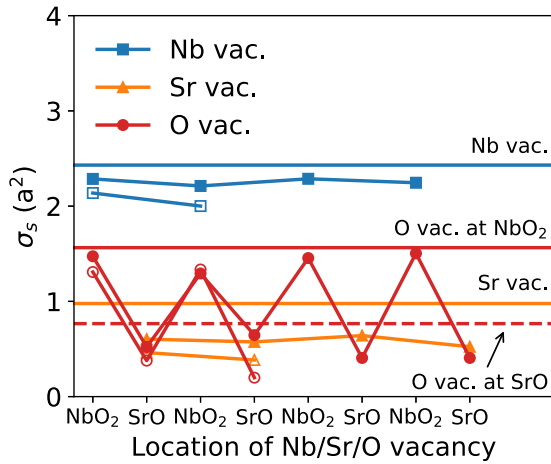


FIG. 5. Scattering cross sections of different vacancies in SrNbO₃. The values were evaluated at the Fermi level, and the cross sections are given in units of the unit cell area. Horizontal lines correspond to bulk values and the hollow (filled) markers correspond to scattering from different vacancy locations in two (four) u.c. thick slabs.

vacancies in NbO₂ and SrO layers. Overall, it is clear that in SrNbO₃ the Nb vacancies have the biggest impact on the transport, followed by O vacancies in NbO₂ layers, and finally Sr and O vacancies in SrO layers having negligible impact. Bulk scattering cross sections are $\approx 2.5a^2$ for Nb vacancies, $1.6a^2$ for O vacancies in the NbO₂ layer, $1.0a^2$ for Sr vacancies, and $\approx 0.8a^2$ for O vacancies in SrO layers. For the ultrathin slabs the scattering cross sections are $\approx 2.1a^2$ for Nb vacancies, $1.4a^2$ for O vacancies in the NbO₂ layer, $0.5a^2$ for Sr vacancies, and $\approx 0.5a^2$ for O vacancies in SrO layers. It is interesting to note that the scattering cross sections are generally lower for the slab compared to bulk. This might be due to the discretization in terms of transverse quantization which limits the scattering channels. We further recall that the geometrical cross section, A , is given by the width and height of the slabs as defined by the ionic positions. Therefore, any conduction done by states that extend into the vacuum will not be accounted for by the nominal area, A . This leads to an underestimation of the scattering cross section, σ_s , for thinner slabs. This is another potential reason for the observed reduced scattering cross sections in slabs.

V. ELECTRON TRANSPORT IN *N*-TYPE SrTiO₃

Next we will contrast the results from the metallic SrNbO₃ to semiconducting SrTiO₃, to explore whether the concentration of electrons affects the electron-vacancy scattering in *n*-type SrTiO₃. Intuitively, the total conductance should increase with more electrons. This is exactly what we observe when doping SrTiO₃ with V (for details see Supplemental Material [23]). We here dope with V (instead of, e.g., Nb), since V has 3*d* orbitals like Ti. A systematic shift in the Fermi level is observed when doping with V, and the conduction band gets occupied. In this section, we focus on examining the influence of electron concentration on the scattering mechanism, rather than on the more straightforward relationship between the number of free carriers and the conductance.

A. Bulk conductance in doped SrTiO₃

To illustrate the conductive properties of *n*-type bulk SrTiO₃, we present the conductance of SrTiO₃ with $0.1e/u.c.$ in Fig. 6(a). The pristine system resembles SrNbO₃, however with a shift in Fermi level and a smaller conduction band width. The narrower bands of SrTiO₃ are expected due to the more localized nature of the Ti 3*d* states compared to the Nb 4*d* states. Interestingly, in comparison to SrNbO₃, the decrease in conductance caused by a Sr vacancy in SrTiO₃ is significantly higher (by $\approx 200\%$ for $0.1e/u.c.$), whereas the scattering resulting from an O vacancy is even less pronounced. Similar to the observations in SrNbO₃, the vacancy at the *B* site continues to have the most substantial effect on the conductance.

B. Slab conductance in doped SrTiO₃

Next, the transport in two u.c. thick slabs of SrTiO₃ doped with $0.1e/u.c.$ is investigated. Like in the case of SrNbO₃, we only present the transport in slabs with vacancies placed in or near the TiO₂ termination layer, i.e., vacancies in the first unit cell in the *y* direction (see Fig. 1). The conductances are presented in Fig. 6(b). The comparison between the bulk SrTiO₃ and the two u.c. thick slab of SrTiO₃ shows a similarity to the comparison observed between bulk and slab SrNbO₃. In both cases, confinement leads to distinct steps in conductance, but the overall trends regarding the impact of different types of vacancies remain consistent. The somewhat remarkable finding that the O vacancies now play a minor role can be understood from the Fermi level position being at the band edge, rather than well inside the band as in SrNbO₃. At higher energies the O vacancy scattering comes into play. In essence, there appears to be no qualitative difference in electron-vacancy scattering when comparing bulk and slab forms of SrTiO₃, except we note that the onset of O vacancy scattering is much earlier with respect to energy in the slab compared to bulk.

C. Doping and scattering cross sections in SrTiO₃

To quantitatively investigate the relation between scattering cross section and carrier concentration, we systematically evaluated the conductance of SrTiO₃ with varying doping and defect configurations. In Fig. 7, the scattering cross sections are shown vs carrier concentration for bulk, two u.c., and three u.c. thick SrTiO₃, respectively. The layered resolved scattering cross sections are shown in the slab cases. We first summarize the finding from the bulk results (dotted lines in Fig. 7), then move over to nuances in the slab results. While we here focus on scattering at Fermi level, energy resolved conductances vs doping for the defective bulk systems can be found in Supplemental Material [23]. In highly doped bulk ($1.0e/u.c.$), the order and magnitudes of the scattering cross sections are similar to those of SrNbO₃. Specifically, Ti vacancies result in the largest resistance and scattering cross section, followed by O vacancies in the TiO₂ layer, and finally Sr vacancies. Interestingly, reducing the number of electrons causes the scattering cross section to increase for Ti and Sr vacancies. The scattering by O vacancies is initially reduced with a decrease in the number of electrons followed by an

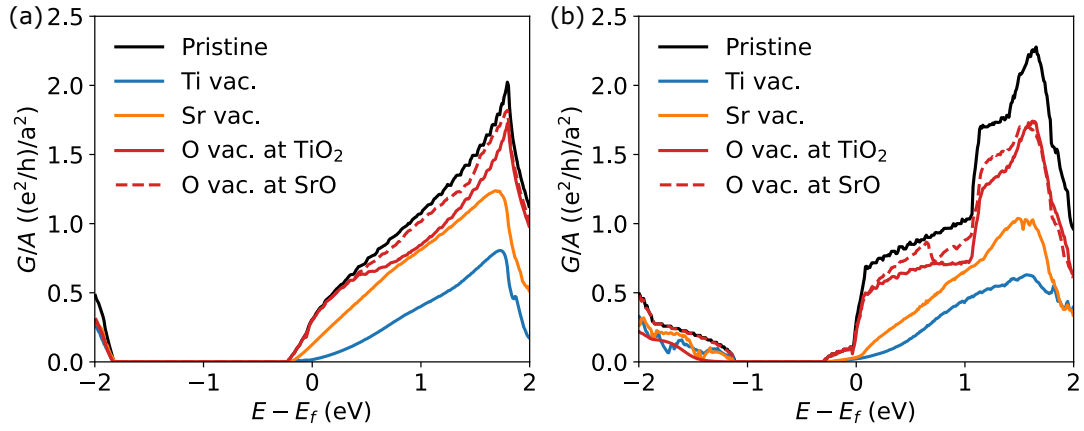


FIG. 6. Conductance per unit cell area for different vacancy configurations. (a) Bulk SrTiO₃ doped with $0.1e/u.c.$ with periodic boundary conditions in the transverse (xy) directions and a three u.c. supercell. (b) Two unit cell thick slab configuration of SrTiO₃ doped with $0.1e/u.c.$ The vacancies are placed in the first unit cell counting from the TiO₂ termination layer. Periodicity is applied in the transverse (x) direction and a three u.c. supercell.

increase between $\approx 0.10e/u.c.$ and $0.02e/u.c.$ We note that the bottom of the conduction band can be more sensitive to finite sampling effects, and while we smear the transmission functions to evaluate the cross sections we do expect larger inaccuracies in the lower doped systems. Between $0.10e/u.c.$ and $0.50e/u.c.$ the scattering cross section is below $0.65a^2$. It is noteworthy that the scattering cross sections of Ti and Sr vacancies increase significantly from $2.2a^2$ and $0.7a^2$, respectively, at $1.0e/u.c.$ up to $9a^2$ at a lower doping of $0.02e/u.c.$ Note that the bulk geometrical cross section is $A = 3a \times 3a = 9a^2$, i.e., a scattering cross section of $9a^2$ indicates that the transport through the defective system is zero at this defect density, and that σ_s will be beyond $9a^2$. This is observed for the lowly doped bulk SrTiO₃ with Sr and Ti vacancies.

Numerous similarities are observed when we compare the outcome of the two u.c. doped SrTiO₃ with its bulk counterparts. For instance, there is an increase in scattering due to Sr and Ti vacancies with a decrease in carrier concentration. Note that in two u.c. the geometrical cross section is $A = wh =$

$3a \times 2a = 6a^2$, where the w and h are the widths and heights of the computational cell, respectively. Hence, the “truncated” values ($6a^2$) indicate defect configurations with vanishing transmission. Interestingly, the O vacancy scattering is enhanced if the vacancy is placed in the TiO₂ termination layer compared to the TiO₂ layer near the SrO termination layer (noted as “2 u.c., vac. in 1st u.c.” and “2 u.c., vac. in 2nd u.c.,” respectively, in Fig. 7). Furthermore, it seems that the Ti vacancy scattering is suppressed in the TiO₂ termination compared to bulk and other layers. These trends are also present in the three u.c. and four u.c. (not shown here) thick slabs. This indicates that the oxygen states near the TiO₂ termination have a greater impact on electronic transport, compared to oxygen states in bulk and near SrO termination layers. Hence, there is a shift in importance from Ti vacancies to O vacancies when comparing the TiO₂ termination layers with bulk and other layers. This was not observed in SrNbO₃ which indicates that the electron vacancy is a combination of location *and* carrier concentration.

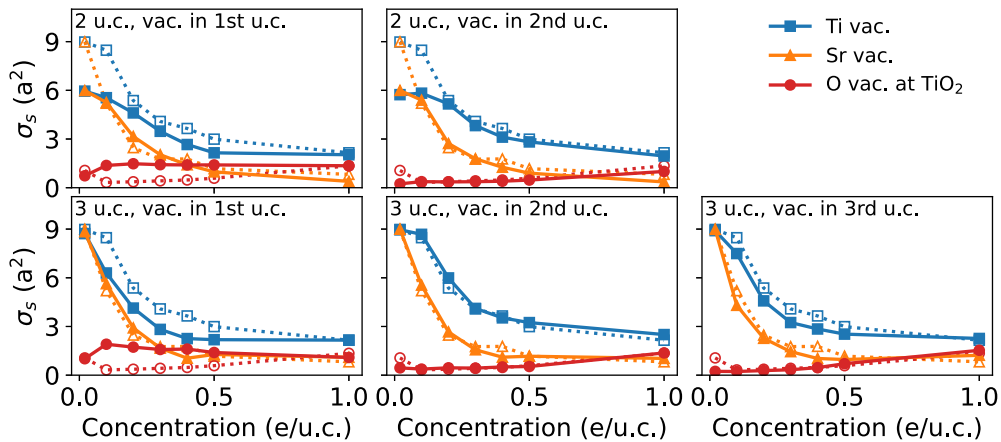


FIG. 7. Scattering cross section due to vacancies in doped SrTiO₃ with varying number of extra electrons. The two rows correspond to two u.c. and three u.c. thick slabs, respectively. Bulk values are included as dotted lines with hollow markers. The columns correspond to the different layers in which the vacancies are placed (from TiO₂ termination to the left to the SrO termination to the right). Note, that the geometrical cross section of the two u.c. slab differs from the others ($A = \text{width} \times \text{height}$).

From the four u.c. thick slabs of doped SrTiO₃, we observe similar trends in the scattering found in the two and three u.c. thick slabs. For SrTiO₃ with 0.02e/u.c., the scattering cross sections of the Sr and Ti vacancies placed in the first unit cell (counting from TiO₂ termination) are 10.3a² and 10.2a², respectively. These values are smaller than the geometrical cross-sectional area of $A = wh = 3a \times 4a = 12a^2$, which indicates that the scattering cross sections are in fact below 12a² for these configurations. The other vacancy locations still exhibit values of 12a² for SrTiO₃ with 0.02e/u.c., which indicates that the cross sections are larger than 12a² for Sr and Ti vacancies placed in layers further away from the TiO₂ termination unit cell.

These findings indicate that while TiO₂ termination layers seem more sensitive to O vacancies, the majority of vacancy configurations in slabs are quite similar to the bulk counterparts. More generally, the findings from this section suggest that to a large extent it is the electron concentration, and not confinement effects, that determines the impact of the electron-vacancy scattering in these oxides. Varying the carrier concentration shifts the relative importance of the different vacancies. Furthermore, the shift in relative importance of the different vacancies can have two origins: either the atomic orbitals involved in the transport are changed with Fermi level shift or the electrostatic screening of the vacancy potential is sensitive to the number of electrons. To understand the origin, we returned to the atomistic PDOS of bulk SrTiO₃ (see Fig. 2) and examined the energy resolved conductances of bulk SrTiO₃ with various vacancies (see Supplemental Material [23]). As discussed in Sec. III, the conduction bands of SrTiO₃ have a strong Ti character, followed by O and a negligible Sr character [see Fig. 2(b)]. While Ti ions have large effect on transport and large contribution to conduction states, Sr vacancies are the opposite. Sr vacancies have large impact on transport; however, the Sr PDOS is negligible in the conduction bands. This is further displayed in Supplemental Material [23], where the energy resolved conductance of bulk SrTiO₃ with Sr vacancy is shown for varying doping. The conductance of the defective system is drastically reduced when the electron doping is reduced, while the Sr PDOS remains negligible throughout the conduction band (see Fig. 2). This indicates that the change in scattering cross section is not simply due to a change in which states are involved in the transport, but also how the electrons interact with the defect potential, especially in the case of Sr vacancies.

VI. VACANCIES AND OXIDE THIN FILMS

This theoretical study was inspired by the frequent references to vacancies, particularly oxygen vacancies, as crucial factors in explaining the electrical behavior of thin film oxides. On one side, vacancies can serve as dopants (for example, oxygen vacancies in SrTiO₃ make it *n* type), but on the other, they disrupt the periodic lattice, leading to electron scattering. The literature has yet to address how strongly a single vacancy scatters electrons in conducting perovskite oxides and, importantly, what factors affect the strength of this scattering. Experimental trends often show a reduction of mobility and conductivity with respect to decreased thickness.

Interestingly, we observe that the TiO₂ terminated surfaces of lowly doped SrTiO₃ are more sensitive to O vacancies (more than six times larger scattering cross section) compared to other layers and bulk counterparts. This is accompanied by a reduction of the scattering cross section of the Ti vacancies in the TiO₂ terminated surfaces. This indicates that the electron-vacancy scattering in TiO₂ terminated surfaces of SrTiO₃ might be unique, and that O vacancies might become stronger scattering centers in these surfaces. This was not observed in SrNbO₃ (and highly doped SrTiO₃), which suggests that the electron-vacancy scattering is sensitive to an interplay between the number of free electrons and to the surface effects. Moreover, the vacancy formation can be substrate driven (e.g., via strain [29]), which could make the ultrathin films more prone to vacancies and, therefore, result in a higher total electron scattering and reduced mobility.

We have shown that the electron concentration in SrTiO₃ plays a significant role in determining the strength of electron-vacancy scattering, particularly for Sr and Ti vacancies. Given that experimentally measured carrier concentrations frequently vary with film thickness, it leads us to speculate that thin film oxides might exhibit increased resistivity due to a decrease in free electrons, but importantly perhaps also due to an increased electron-vacancy scattering strength due to the decreased carrier concentration. In other words, reducing the carrier concentration could be twofold: mainly by directly reducing the number of free carriers, and secondly by increasing the *A*- and *B*-site electron-vacancy scattering strength. While O vacancies are often depicted as mobility-limiting scattering centers, we surprisingly find that the scattering cross section of a O vacancy is often smaller than both *A*- and *B*-site vacancies (except for SrNbO₃ and highly doped SrTiO₃ where all vacancies have relatively small cross sections). This could be part of the reason why the electron gas at, e.g., the LaAlO₃/SrTiO₃ interface has such a high mobility [30] even though O vacancies play a crucial role in the formation of the electron gas [9]. That would suggest that the gain in extra electrons due to an oxygen vacancy outweighs the additional electron scattering thanks to the small scattering cross section of the oxygen vacancy, as indicated by our calculations on doped SrTiO₃. This competition is, however, dependent on the number of free carriers and the scattering cross sections for the vacancies in those specific heterostructures.

We want to point out that in this paper we have only considered single vacancies, i.e., the resistances and scattering cross sections are due to *one* vacancy in the transport direction. In reality, there will likely be a distribution of vacancies between the source and drain that lead to a total electrical resistance or mobility. In the following, we estimate the vacancy limited electron mobility for different vacancy and doping conditions. This is done to contextualize our findings and to ease the comparison between our predictions and experimental data.

A. Vacancy limited mobility

A simple estimate of a mean free path (MFP), ℓ , based on independent defects can be found from the scattering cross section $\sigma_s(i)$ and impurity concentration, N_i , of the different

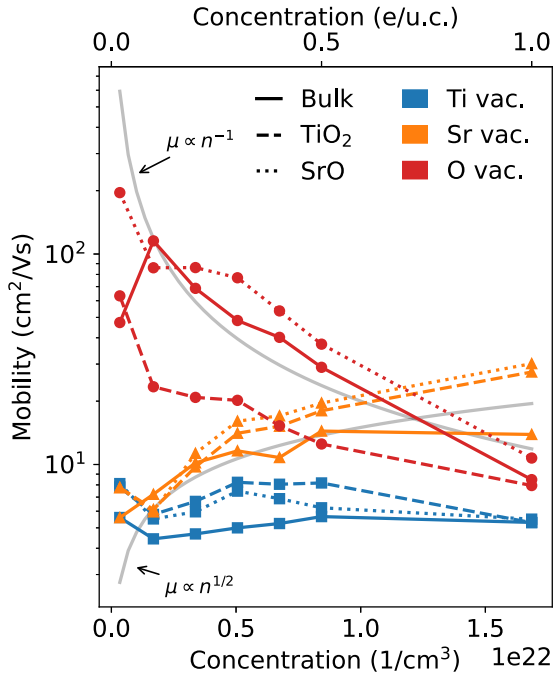


FIG. 8. Vacancy limited electron mobility of SrTiO₃ as a function of carrier concentration. The vacancy concentrations were set to $1 \times 10^{21} \text{ cm}^{-3}$. The solid lines correspond to bulk results, while dashed/dotted lines correspond to two u.c. results with vacancies placed in unit cells closest to the TiO₂/SrO termination layer. The gray lines are included as guides for the eye.

vacancy species i [28,31]:

$$\ell \approx 1 / \sum_i [N_i \sigma_s(i)]. \quad (5)$$

Using this and the pristine transmission $T_0(E_F)$ one may further obtain an estimate for the conductivity of the metallic systems:

$$\sigma \approx \frac{2e^2}{h} \frac{T_0(E_F)}{A} \ell. \quad (6)$$

From the conductivity, the vacancy limited mobility can be estimated as $\mu = \sigma/ne$. Figure 8 presents the vacancy limited mobility of SrTiO₃ as a function of electron concentration. The MFPs were evaluated with vacancy concentrations $N_i = 1 \times 10^{21} \text{ cm}^{-3}$ for each vacancy type. Only one vacancy type was considered at a time. Note that $\mu \propto 1/N_i$, i.e., from Fig. 8 the mobility can be scaled to represent other vacancy concentrations depending on experimental conditions (typical oxygen vacancy concentrations are between 1×10^{17} and $1 \times 10^{22} \text{ cm}^{-3}$ [2]). For the given vacancy concentrations the predicted vacancy limited mobilities are between 4 and 200 cm^2/Vs . This range is comparable with experimental values for SrNbO₃ [12] and SrTiO₃ in the high doping limit [32]. This indicates that real films typically have a vacancy concentration comparable to $1 \times 10^{21} \text{ cm}^{-3}$. Note, this is excluding any other types of defects and electron scattering mechanisms, i.e., the vacancy concentration is an overestimation. From Fig. 8, it is seen that the Ti vacancies limit the electron mobility the most (as expected by the large scattering cross sections). The Ti vacancy limited mobility remains almost

constant with respect to electron concentration. Sr vacancies have a slightly smaller impact on mobility, $\approx 200\%$ higher mobility than Ti vacancy, except for in lowly doped systems. The Sr vacancies go from being a small limitation on the mobility in highly doped systems, to being very important in lowly doped systems. This change is $\approx 200\%$ going from a carrier concentration of 3.4×10^{20} to $1.6 \times 10^{22} \text{ cm}^{-3}$, which indicates the sensitivity of electron concentration on the role of Sr vacancies. Furthermore, the role of O vacancies is also sensitive to electron concentration. The O vacancy limited mobility decreases by an order of magnitude, when the carrier concentration increases from 3.4×10^{20} to $1.6 \times 10^{22} \text{ cm}^{-3}$. While the Ti and Sr vacancy limited mobilities of two u.c. slabs are comparable to the bulk counterparts, the O vacancy placed in the TiO₂ termination layer sticks out (red dashed line in Fig. 8). The mobility can be up to six times lower when the O vacancy is located in a TiO₂ termination layer compared to bulk. Furthermore, the SrO termination layer is less sensitive to O vacancies compared to bulk. This indicates that TiO₂ terminated SrTiO₃ surfaces might be more prone to reduced mobility due to O vacancies compared to bulk and SrO terminated SrTiO₃. Finally, we note that since the mobility with respect to electron concentration is different for the anion and cation vacancies (as highlighted by the gray lines in Fig. 8), mobility vs concentration trends could potentially be used to understand which vacancies are present and also what the vacancy concentrations are.

VII. OUTLOOK

Transport calculations based on DFT have here been used to study the role of different vacancies on the electronic transport in oxides. While we have been able to estimate the scattering strengths and electron mobilities due to vacancies, we have made various simplifications along the way. In no particular order, it could be insightful to investigate the effect of static vs dynamic electron correlations, e.g., by Hubbard U corrections and beyond, or to include temperature effects by considering electron-phonon scattering. Furthermore, including spin degree of freedom could be relevant for understanding how magnetic moments are stabilized—and perhaps how to generate spin currents via different scattering mechanisms. These are topics for future studies that hopefully will further enrich the understanding of electron transport in oxides.

VIII. CONCLUSION

The effect of vacancies on the electronic transport in bulk and ultrathin slabs of SrNbO₃ and n -type SrTiO₃ has been investigated. The transport problem was investigated numerically using DFT-NEGFs. We find that pristine bulk and slabs are conductive and the inclusion of vacancies reduces the conductance, as expected. Furthermore, we see that while the order in terms of scattering strength among the different defects is roughly preserved the strength in SrTiO₃ slabs—especially of O vacancies—depends strongly on position and doping. In particular, it can in some cases be significantly higher than the bulk estimate. As an example, O vacancy placed in TiO₂ termination layers has scattering cross

sections approximately six times larger than bulk counterparts in lowly doped SrTiO₃. Moreover, we observe a strong increase in the scattering cross section of both *A*- and *B*-site vacancies when reducing the electron concentration in *n*-type SrTiO₃. These findings could be part of the explanation for the poor electrical performance of some thin film oxides, especially in conditions where the carrier concentration is depleted (which is often observed). Surprisingly, while the scattering cross sections of O vacancies are comparable to the values of *A*- and *B*-site vacancies in SrNbO₃ and heavily doped SrTiO₃, their relative scattering strengths reduce substantially in lowly doped SrTiO₃. This could render O vacancies rather unimportant scattering centers in some oxides, especially since they also contribute with additional free electrons, which enhances the total conductance. By examining PDOS, we speculate that the change in relative importance of the vacancies is related to

a change in the screening with doping and not due to a change in orbital character of the conduction states.

ACKNOWLEDGMENTS

This work has been supported by Independent Research Fund Denmark Grant No. 8048-00088B and Innovation Fund Denmark Grant No. 1045-00029B. N.P. acknowledges the support of Novo Nordisk Foundation Challenge Programme 2021: “Smart nanomaterials for applications in life-science,” BIOMAG Grant No. NNF21OC0066526; support from European Research Council Advanced “NEXUS” Grant No. 101054572; and support from the Danish Council for Independent Research Technology and Production Sciences for DFF-Research Project 3 (Grant No. 00069B).

-
- [1] J. Son, P. Moetakef, B. Jalan, O. Bierwagen, N. J. Wright, R. Engel-Herbert, and S. Stemmer, Epitaxial SrTiO₃ films with electron mobilities exceeding 30,000 cm² V⁻¹ s⁻¹, *Nat. Mater.* **9**, 482 (2010).
- [2] F. Gunkel, D. V. Christensen, Y. Z. Chen, and N. Pryds, Oxygen vacancies: The (in)visible friend of oxide electronics, *Appl. Phys. Lett.* **116**, 120505 (2020).
- [3] D.-S. Park *et al.*, The emergence of magnetic ordering at complex oxide interfaces tuned by defects, *Nat. Commun.* **11**, 3650 (2020).
- [4] L. Hu, X. Luo, K. J. Zhang, X. W. Tang, L. Zu, X. C. Kan, L. Chen, X. B. Zhu, W. H. Song, J. M. Dai, and Y. P. Sun, Oxygen vacancies-induced metal-insulator transition in La_{2/3}Sr_{1/3}VO₃ thin films: Role of the oxygen substrate-to-film transfer, *Appl. Phys. Lett.* **105**, 111607 (2014).
- [5] H. O. Jeschke, J. Shen, and R. Valentí, Localized versus itinerant states created by multiple oxygen vacancies in SrTiO₃, *New J. Phys.* **17**, 023034 (2015).
- [6] Z. Liao, F. Li, P. Gao, L. Li, J. Guo, X. Pan, R. Jin, E. W. Plummer, and J. Zhang, Origin of the metal-insulator transition in ultrathin films of La_{2/3}Sr_{1/3}MnO₃, *Phys. Rev. B* **92**, 125123 (2015).
- [7] Y. Ha and S. Lee, Oxygen-vacancy-endurable conductors with enhanced transparency using correlated 4d²SrMoO₃ thin films, *Adv. Funct. Mater.* **30**, 2001489 (2020).
- [8] H. Okuma, Y. Katayama, K. Otomo, and K. Ueno, Transport properties around the metal-insulator transition for SrVO₃ ultrathin films fabricated by electrochemical etching, *Phys. Rev. B* **105**, 045138 (2022).
- [9] Z. Q. Liu, C. J. Li, W. M. Lü, X. H. Huang, Z. Huang, S. W. Zeng, X. P. Qiu, L. S. Huang, A. Annadi, J. S. Chen, J. M. D. Coey, T. Venkatesan, and Ariando, Origin of the two-dimensional electron gas at LaAlO₃/SrTiO₃ interfaces: The role of oxygen vacancies and electronic reconstruction, *Phys. Rev. X* **3**, 021010 (2013).
- [10] S. A. Lee, S. Oh, J. Lee, J. Y. Hwang, J. Kim, S. Park, J. S. Bae, T. E. Hong, S. Lee, S. W. Kim, W. N. Kang, and W. S. Choi, Tuning electromagnetic properties of SrRuO₃ epitaxial thin films via atomic control of cation vacancies, *Sci. Rep.* **7**, 11583 (2017).
- [11] G. Wang, Z. Wang, M. Meng, M. Saghayezhian, L. Chen, C. Chen, H. Guo, Y. Zhu, E. W. Plummer, and J. Zhang, Role of disorder and correlations in the metal-insulator transition in ultrathin SrVO₃ films, *Phys. Rev. B* **100**, 155114 (2019).
- [12] D. Oka, Y. Hirose, S. Nakao, T. Fukumura, and T. Hasegawa, Intrinsic high electrical conductivity of stoichiometric SrNbO₃ epitaxial thin films, *Phys. Rev. B* **92**, 205102 (2015).
- [13] Y. Park, J. Roth, D. Oka, Y. Hirose, T. Hasegawa, A. Paul, A. Pogrebnjakov, V. Gopalan, T. Birol, and R. Engel-Herbert, SrNbO₃ as a transparent conductor in the visible and ultraviolet spectra, *Commun. Phys.* **3**, 102 (2020).
- [14] J. M. Ok, N. Mohanta, J. Zhang, S. Yoon, S. Okamoto, E. S. Choi, H. Zhou, M. Briggeman, P. Irvin, A. R. Lupini, Y.-Y. Pai, E. Skoropata, C. Sohn, H. Li, H. Miao, B. Lawrie, W. S. Choi, G. Eres, J. Levy, and H. N. Lee, Correlated oxide Dirac semimetal in the extreme quantum limit, *Sci. Adv.* **7**, eabf9631 (2021).
- [15] A. Chatterjee, Z. Lan, D. V. Christensen, F. Bauitti, A. Morata, E. Chavez-Angel, S. Sanna, I. E. Castelli, Y. Chen, A. Tarancon, and N. Pryds, On the thermoelectric properties of Nb-doped SrTiO₃ epitaxial thin films, *Phys. Chem. Chem. Phys.* **24**, 3741 (2022).
- [16] M. Zhu, P. Li, L. Hu, R. Wei, J. Yang, W. Song, X. Zhu, and Y. Sun, Thickness dependence of metal-insulator transition in SrMoO₃ thin films, *J. Appl. Phys.* **132**, 075303 (2022).
- [17] J. P. Perdew, K. Burke, and M. Ernzerhof, Generalized gradient approximation made simple, *Phys. Rev. Lett.* **77**, 3865 (1996).
- [18] V. Rosendal, W. H. Brito, M. Radovic, A. Chikina, M. Brandbyge, N. Pryds, and D. H. Petersen, Octahedral distortions in SrNbO₃: Unraveling the structure-property relation, *Phys. Rev. Mater.* **7**, 075002 (2023).
- [19] R. Poloni, J. Íñiguez, A. García, and E. Canadell, An efficient computational method for use in structural studies of crystals with substitutional disorder, *J. Phys.: Condens. Matter* **22**, 415401 (2010).
- [20] A. García *et al.*, SIESTA: Recent developments and applications, *J. Chem. Phys.* **152**, 204108 (2020).
- [21] M. Brandbyge, J.-L. Mozos, P. Ordejón, J. Taylor, and K. Stokbro, Density-functional method for nonequilibrium electron transport, *Phys. Rev. B* **65**, 165401 (2002).

- [22] N. Papior, N. Lorente, T. Frederiksen, A. García, and M. Brandbyge, Improvements on non-equilibrium and transport Green function techniques: The next-generation TRANSIESTA, *Comput. Phys. Commun.* **212**, 8 (2017).
- [23] See Supplemental Material at <http://link.aps.org/supplemental/10.1103/PhysRevB.109.205129> for comparison between LCAO and PW, impact of ionic relaxation, and effect of doping on conductance of SrTiO₃.
- [24] N. Papior, *sisl*: v13.0 (2023).
- [25] C. Bigi, P. Orgiani, J. Sławińska, J. Fujii, J. T. Irvine, S. Picozzi, G. Panaccione, I. Vobornik, G. Rossi, D. Payne, and F. Borgatti, Direct insight into the band structure of SrNbO₃, *Phys. Rev. Mater.* **4**, 025006 (2020).
- [26] A. Chikina, V. Rosendal, H. Li, E. B. Guedes, M. Caputo, N. C. Plumb, M. Shi, D. H. Petersen, M. Brandbyge, W. H. Brito, E. Pomjakushina, V. Scagnoli, J. Lyu, M. Medarde, E. Skoropata, U. Staub, S.-W. Huang, F. Baumberger, N. Pryds, and M. Radovic, Provoking topology by octahedral tilting in strained SrNbO₃, [arXiv:2311.06072](https://arxiv.org/abs/2311.06072).
- [27] T. Markussen, R. Rurali, A.-P. Jauho, and M. Brandbyge, Scaling theory put into practice: First-principles modeling of transport in doped silicon nanowires, *Phys. Rev. Lett.* **99**, 076803 (2007).
- [28] T. Markussen, R. Rurali, X. Cartoixà, A.-P. Jauho, and M. Brandbyge, Scattering cross section of metal catalyst atoms in silicon nanowires, *Phys. Rev. B* **81**, 125307 (2010).
- [29] U. Aschauer, R. Pfenninger, S. M. Selbach, T. Grande, and N. A. Spaldin, Strain-controlled oxygen vacancy formation and ordering in CaMnO₃, *Phys. Rev. B* **88**, 054111 (2013).
- [30] A. Ohtomo and H. Y. Hwang, A high-mobility electron gas at the LaAlO₃/SrTiO₃ heterointerface, *Nature (London)* **427**, 423 (2004).
- [31] K. Saloritta, A. Uppstu, A. Harju, and M. J. Puska, *Ab initio* transport fingerprints for resonant scattering in graphene, *Phys. Rev. B* **86**, 235417 (2012).
- [32] F. Trier, D. V. Christensen, and N. Pryds, Electron mobility in oxide heterostructures, *J. Phys. D* **51**, 293002 (2018).